Atomic Layer Deposition-Assisted Synthesis of Embedded Vanadia Catalysts

Philip Ruff, Leon Schumacher, Simone Rogg, Christian Hess*

Eduard-Zintl-Institut für Anorganische und Physikalische Chemie, Technische Universität Darmstadt, Alarich-Weiss-Str. 8, 64287 Darmstadt, Germany

*hess@pc.chemie.tu-darmstadt.de

TOC graphic

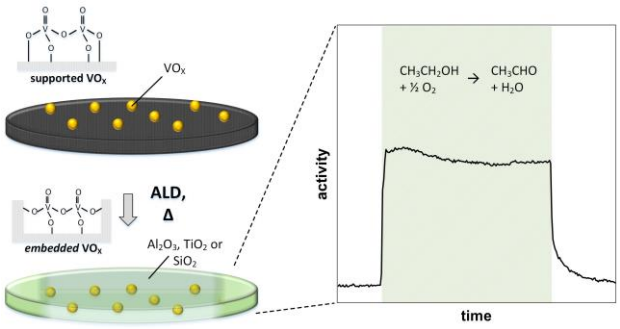
supported VO_x
VO_x
ALD,
Δ
embedded VO_x
Al_2O_3, TiO_2 or
SiO_2
CH_3CH_2OH
+ ½ O_2
CH_3CHO
+ H_2O
activity
time

Abstract

Catalyst–support interactions are known to be of great importance for the performance of supported oxide catalysts such as supported vanadia. With the aim of enhancing the oxide-support interactions we propose a strategy for the controlled synthesis of embedded oxide catalysts using atomic layer deposition (ALD). As demonstrated for vanadia (VO_x), the synthesis is based on the sequential deposition of VO_x and the 'support' material (Al_2O_3, SiO_2, TiO_2) onto graphene oxide, which serves as a sacrificial carrier matrix facilitating the embedding of VO_x, followed by template removal by calcination or ozone treatment. Detailed characterization of the synthesis process and the final catalysts is carried out using multiple spectroscopic (Raman, UV-vis, XPS), thermogravimetric, and electron-microscopic (TEM, EELS) analysis. The successful formation of a VO_x–support interphase is confirmed by UV Raman spectroscopy. Despite the high loadings (L_V > monolayer coverage) of accessible sites, the embedded VO_x is present in a dispersed state in the case of the ozonolyzed samples. Structural models are proposed to account for the observed behavior. The activity of the embedded VO_x catalysts is verified in the oxidative dehydrogenation (ODH) of ethanol and compares favorably with reported data on conventional supported catalysts. Compared to the literature, the ozonolyzed VO_x/Al_2O_3 catalysts show a significantly improved performance, whereas the VO_x/SiO_2 catalysts define a benchmark. Our results demonstrate the feasibility of rational catalyst engineering of supported oxide catalysts.

Keywords: atomic layer deposition, vanadia, embedded catalyst, oxidative dehydrogenation, sacrificial template, graphene oxide

1. Introduction

Vanadia supported on various metal oxides such as Al_2O_3, TiO_2 and SiO_2 has been studied extensively as catalyst for selective oxidation reactions of organic compounds such as alkanes, alkenes, alcohols, aldehydes, and ketones, amongst many others.[1-20] A well-known problem of supported metal oxide and metal catalysts is their decreasing activity and selectivity over time, which is related to a loss of active species due to sintering or volatility during the reaction.[15,21-24] Thus, it is desirable to increase the lifetime of a catalyst by improving its stability in order to maintain its activity and selectivity over many catalytic cycles. To this end, different strategies have been outlined for the fabrication of stabilized and well-defined nanostructured metal catalysts.[21,25-27] In this context, atomic layer deposition (ALD) offers outstanding process control owing to its self-limiting nature.[28] In combination with different surface passivation techniques, such as templating using proteins or single molecules, as well as lithography, area-selective ALD allows the nanoscale structuring of planar and even highly porous substrates,[28-30] which may serve as catalyst supports.

There are basically two major strategies for the ALD-based synthesis of nanostructured metal catalysts. On the one hand, bottom-up approaches are based on the deposition of metal nanoparticles on a support followed by the deposition of another material serving as a protective overcoating.[26,27] On the other hand, templating techniques allow the fabrication of confined metal nanoparticles, by depositing metal nanoparticles on a sacrificial substrate, subsequently applying an overcoating and finally removing the template.[21,25,27] There are various modifications of the two techniques, including the combination of different metals and oxides as well as the application of a cocatalyst, with the aim of generating synergetic effects.[25-27] Catalytic experiments with these catalysts have yielded an improved sintering-resistance compared to conventional supported metal nanoparticles.[21,31-32] To our knowledge, the template-based ALD approach has been applied exclusively to supported metal catalysts.

Supported oxide catalysts e.g. VO_x catalysts are commonly prepared by using impregnation methods. Alternatively, gas-phase deposition techniques such as chemical vapor deposition (CVD) or ALD can be used to graft VO_x onto a supporting surface. The feasibility of producing highly dispersed VO_x on different substrates by using ALD has been reported previously.[33-36] Furthermore, catalysts prepared by one of the two methods, impregnation and gas-phase deposition, have already been studied in oxidative dehydrogenation (ODH) reactions of methanol and ethanol regarding structural and catalytic properties.[34,36]

In this work, we present an approach enabling the controlled synthesis of embedded metal oxide catalysts, with the aim of increasing catalyst–support interactions compared to conventional supported metal oxide catalysts prepared by impregnation or gas-phase deposition. The feasibility of the presented strategy for rational catalyst engineering is demonstrated for a series of vanadia (VO_x) catalysts. A scheme outlining the catalyst preparation is given in Figure 1. In a first step, VO_x is dispersed on graphene oxide (GO) using atomic layer deposition (ALD). GO serves as a sacrificial support providing functional groups for metal oxide ALD and is easily decomposable by thermal treatment. The dispersed VO_x species are then ALD–coated with different metal oxides (SiO_2, Al_2O_3, TiO_2), conserving the dispersion and thus the active VO_x sites within. Embedded VO_x catalysts supported within a metal oxide matrix are then obtained upon removal of graphene oxide by i) calcination in static air or ii) treatment with ozone. Using wet chemical methods, it is not possible to obtain embedded VO_x catalysts in such a controlled fashion as by ALD. For example, adding a vanadium–containing precursor during the synthesis of the support may yield some embedded VO_x, but mainly VO_x fully encapsulated within the supporting matrix. Thus, the feasibility of a targeted preparation of embedded and accessible VO_x species is directly linked to the unique nature of the ALD process, which allows a high initial dispersion of VO_x on the one hand and conformal overcoating on the other. Besides the details of the synthesis process, we address the influence of the template-removal method on

the structural and catalytic properties of the embedded VO_x catalysts during the ODH of ethanol.

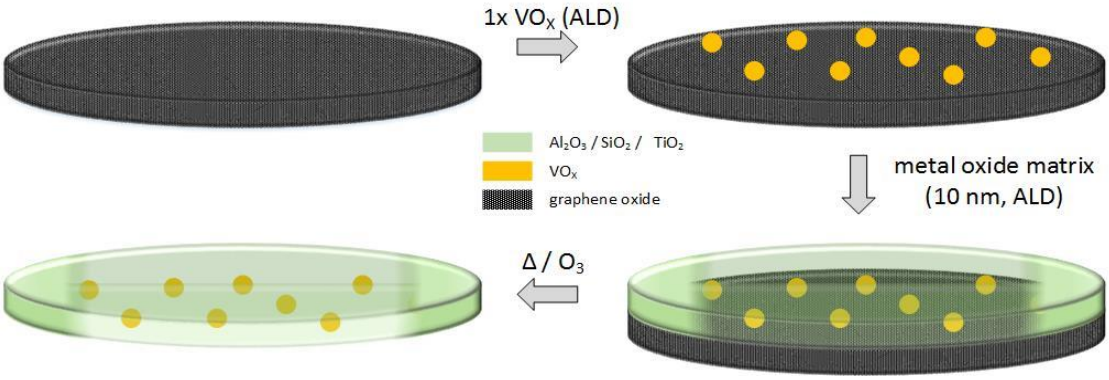

Figure 1. Schematic representation of the synthesis of embedded VO_x catalysts including the dispersion of VO_x on GO oxide ALD, the ALD of Al_2O_3, SiO_2, or TiO_2 serving as supporting metal oxide matrix, and the thermal decomposition of the sacrificial GO template by calcination or reaction with ozone.

2. Experimental Section

2.1. Synthesis of Multilayered Graphene Oxide. Graphene oxide (GO) was synthesized according to the literature.[37] Briefly, 4 g of graphite powder (Alfa Aesar, synthetic, grain size 7–11 μm, 99%) was added to 92 mL of concentrated sulfuric acid (H_2SO_4) in an ice bath. Subsequently, 12 g $KMnO_4$ was added slowly under continuous stirring, taking care that the temperature did not exceed 20°C. The mixture was then stirred for 30 min at 40°C in an oil bath, whereupon 200 mL of deionized water was added and the mixture was heated to 95°C for 15 min. Finally, another 600 mL deionized water and 20 mL H_2O_2 (30%) was added dropwise, causing the color to change from brown to yellow.

For purification the mixture was stirred with 2 L of 10% hydrochloric acid (HCl) for 30 min and subsequently allowed to rest for several hours, allowing the graphite oxide to settle to the bottom. The supernatant was then decanted and the precipitate resuspended in 2 L of 10% HCl. This procedure was repeated several times, first with 10% HCl and then later with deionized water.

Multilayered GO was then obtained upon exfoliation of the graphite oxide by using sonication in deionized water. The aqueous GO suspension was then dried at 40°C, ground to obtain a black powder, and dried in vacuum at room temperature.

2.2. Thermal Metal-Oxide ALD. Thermal ALD of VO_x, SiO_2, Al_2O_3, and TiO_2 was carried out using a custom–made stainless steel ALD reactor using the precursors $VOCl_3$ (Sigma-Aldrich, 99.9%), $SiCl_4$ (Sigma-Aldrich, 99.9%), $Al(CH_3)_3$ (Sigma-Aldrich, 97%), $TiCl_4$ (Sigma-Aldrich, 99.9%), and H_2O. During SiO_2 depositions pyridine was used as a catalyst to assist the reaction of the two precursors $SiCl_4$ and H_2O. For all depositions the reactor walls were heated to 60°C. The base pressure of the ALD reactor was 1.3 Torr. All depositions consisted of the cyclic exposure to the corresponding metal containing precursor and H_2O for 60 s each, separated by purging intervals with N_2 (99.999%, 200 mL/min) for 60 s. Details of the ALD setup have been described previously.[38]

For the synthesis of embedded VO_x catalysts 1 g of multilayered GO was placed in the ALD reactor. In a first step, one ALD cycle of VO_x (exposure ≈ 24 × 10^6 L) was deposited and subsequently ALD coated with 10 nm of SiO_2 (56 cycles), Al_2O_3 (67 cycles), or TiO_2 (295 cycles). A summary of the prepared samples is given in Table 1.

2.3. Template Removal by Calcination. For the thermal decomposition of ALD-coated GO oxide by calcination in static air about 1 g GO was heated from room temperature to 550°C at a rate of 1.5°C/min, and then held at 550°C for 6.5 h.

2.4. Template Removal by Ozone Treatment. The decomposition of ALD-coated GO by reaction with ozone was realized by purging with ozoniferous air (200 mL/min) at 150°C for 10 days. To this end, about 1 g GO was placed in a glass vessel that was coupled to an ozone generator (Heyl Neomeris, LAB 2B) producing 3.5 mg ozone/L air (1.5 g ozone/h).

Table 1. Classification and synthesis procedure for different types of embedded VO_x catalysts; MO = Al_2O_3, SiO_2, TiO_2.

Catalyst name	**VO_x ALD**	**MO ALD**	**Template removal**
1×VO_x-in-Al_2O_3-calc.	1× VO_x	67× Al_2O_3	calcination
1×VO_x-in-Al_2O_3-ozone		67× Al_2O_3	ozone
1×VO_x-in-SiO_2-calc.		56× SiO_2	calcination
1×VO_x-in-SiO_2-ozone		56× SiO_2	ozone
1×VO_x-in-TiO_2-calc.		295× TiO_2	calcination
1×VO_x-in-TiO_2-ozone		295× TiO_2	ozone

2.5. X-Ray Photoelectron Spectroscopy. X-ray photoelectron spectroscopy (XPS) was carried out on an SSX 100 ESCA spectrometer (Surface Science Laboratories Inc.) employing a monochromatic Al K_α X-ray source (1486.6 eV) operated at 9 kV and 10 mA; the spot size was approximately 1 mm × 0.25 mm. Spectra were recorded in the constant analyzer energy (CAE) mode at a 36° detection angle. The base pressure of the analysis chamber was $<10^{-8}$ Torr. Survey spectra (8 measurements) were recorded between 0 and 1100 eV with 0.5 eV resolution, whereas detailed spectra (30 measurements) were recorded with 0.1 eV resolution. To account for sample charging, the C 1s peak of ubiquitous carbon at 284.9 eV was used to correct the binding–energy shifts in the spectra. Data analysis included a Shirley background subtraction and a peak-fit analysis using Gaussian–Lorentzian product functions with 45% Lorentzian share. Atomic concentrations were calculated using the relative sensitivity factors (RSFs) given in Table 2.

Table 2. Relative sensitivity factors used for the XPS analysis.

	C 1s	**Al 2p**	**O 1s**	**Si 2p**	**Ti 2p**	**V 2p**
RSF	0.537	1.000	2.930	0.817	7.810	9.660

2.6. Fourier-Transform Infrared Spectroscopy. Fourier transform infrared (FTIR) transmission spectra of GO/KBr-pellets with a resolution of 0.5 cm^{-1} were obtained from a Bruker Vertex 70 spectrometer equipped with a SiC globar MIR light source and a DLaTGS (deuterated L-alanine doped triglycene sulfate) detector (100 scans). The mirror velocity was 10 kHz. Prior to the measurements, the pellets were dried at 60°C overnight.

2.7. UV-vis Diffuse Reflectance Spectroscopy. UV-vis spectra were measured on a Jasco V-770 UV-visible/NIR spectrophotometer equipped with a Praying Mantis mirror cell and a high temperature reaction chamber (Harrick Scientific Products Inc.). For excitation halogen and deuterium light sources were used. For detection a Peltier cooled PbS detector was employed. Spectra were recorded between 200 and 800 nm with a spectral resolution of 0.5 nm. MgO was used as a white standard. Before the spectra were recorded at room temperature, all samples were dehydrated at 550°C (calcined samples) or 120°C (ozonolyzed samples) for 1 h while being purged with 200 mL/min synthetic air.

2.8. UV Raman Spectroscopy (256.7 nm Excitation). To record UV Raman spectra a tunable Ti:sapphire solid state laser (Indigo-S, Coherent) was used. For the experiments reported here, an excitation wavelength of 256.7 nm was employed. The Raman scattered light was dispersed in a three–stage spectrometer (Princeton Instruments, TriVista 555) used in subtractive mode. The scattered light was detected by a charged coupled device (CCD) camera (Spec10:2kBUV, Princeton Instruments), cooled to –120°C with liquid nitrogen. The spectral resolution was 1 cm^{-1}. Spectra were recorded from dehydrated samples. To this end, the catalysts were placed in a CCR 1000 reaction cell (Linkam Scientific Instruments) equipped with either a CaF_2 or a sapphire window and heated for at least 2 h to 550°C or 120°C for calcined and ozonolyzed samples, respectively. During dehydration the samples were purged with synthetic air (50 mL/min, 8% O_2, 92% N_2). All spectra were recorded at 120°C by irradiating the samples for 600 s with a laser power of 5 mW at a repetition rate of 5 kHz. In addition a cosmic ray filter was employed. All spectra were processed with a background subtraction. The intense band at 315 cm^{-1} (marked with an asterisk) observed in the spectra of the calcined catalysts is a feature arising from the CaF_2 window of the reaction cell. UV Raman spectra of the ozonolyzed catalysts were acquired using a sapphire window. Details of the tunable Raman spectroscopic setup have been described previously.[15,16]

2.9. Visible Raman Spectroscopy (532 nm Excitation). Visible Raman spectra were recorded on a Raman microscope using 532 nm excitation obtained by frequency doubling from a Nd:YAG laser (Cobolt). The Holo Spec f/1.8i spectrometer (Holographic Imaging Spectrograph, Kaiser Optical Systems) was equipped with a transmission grating providing a resolution of 2 cm^{-1}. For detection of the Raman scattered light a Peltier-cooled CCD camera (–40°C) was employed. The light was focused onto the sample with a 50×/long working distance (LWD) objective (Leica, NPlan EP, 456LF/03, 50×/0.5) using a power of 2.5 mW at the sample and an irradiation time of 20 s. Prior to each measurement a new background spectrum was recorded. In addition, a cosmic ray filter was employed. All spectra were processed with a background subtraction.

2.10. Thermogravimetric Analysis. For thermogravimetric analysis (TGA) a TGA/SDTA851-e device (Mettler Toledo) was employed. In order to record TGA curves during the decomposition of ALD-coated GO, samples had synthetic air (200 mL/min) blown over them while being heated from room temperature to 550°C at a rate of 1.5°C/min. The samples were then calcined at 550°C for 6.5 h.

2.11. Physical Characterization. Specific surface areas of GO and the embedded VO_X catalysts were determined on the basis of nitrogen adsorption/desorption isotherms measured on a Thermo Fisher Scientific Surfer BET Analyzer at 77 K and the use of standard multipoint BET (Brunauer-Emmett-Teller) analysis methods. Prior to the measurements all samples were dried in vacuum at room temperature overnight.

2.12. Inductively Coupled Plasma Optical Emission Spectroscopy. Quantification of the vanadium content of the different catalysts was done by the Analytisches Zentrum Berlin-Adlershof GmbH by inductively coupled plasma optical emission spectroscopy (ICP-OES).

2.13. High-Resolution Scanning Transmission Electron Microscopy. Samples were prepared for high-resolution scanning transmission electron microscopy (HRSTEM) by

dispersing a small amount of the powder in ethanol using an ultrasound bath (Bandelin). The dispersion was allowed to settle for a short time to reduce the number of large particles in the dispersion. A droplet of the dispersion was applied to a holey carbon grid (Plano) and allowed to dry. The grid was coated with carbon (Baltec MED010) to avoid charging under the incident electron beam. High resolution TEM images were recorded using a JEOL JEM ARM 200F (JEOL) equipped with an electron energy loss spectroscopy (EELS) detector (Gatan Enfina). The field emission gun was operated at 200 kV.

2.14. Oxidative Dehydrogenation of Ethanol. The reactivity behavior of the as-synthesized embedded VO_x catalysts was tested for ODH of ethanol. To this end, the catalysts were placed in a CCR 1000 reaction cell (Linkam Scientific Instruments) and dehydrated for at least 2 h in synthetic air (8% O_2, 92% N_2; total flow rate: 50 mL/min) at temperatures of 515°C and 190°C for calcined and ozonolyzed samples, respectively. During the catalytic reaction at 190°C the samples were exposed to a feed of 1% ethanol, 8% O_2, and 91% N_2 at a total flow rate of 50 mL/min. Quantitative gas-phase analysis was carried out using FTIR spectroscopy. Spectra were acquired on a Bruker Vertex 70 spectrometer equipped with a LFT 205-20 gas cell (Axiom Analytical Incorporated). Spectra were recorded between 1000 and 4000 cm^{-1} (50 measurements) at a resolution of 4 cm^{-1} using the chromatographic mode of the software OPUS 7.0 (Bruker). To prevent condensation, the cell was heated to 125°C. Based on the recorded spectra, the conversion, selectivity, and turnover frequency (TOF) were calculated according to Equations 1, 2, and 3, respectively.

$$C = \frac{\dot{n}_{EtOH,i} - \dot{n}_{EtOH,f}}{\dot{n}_{EtOH,i}} \quad (1)$$

$$S_{aca} = \frac{\dot{n}_{aca}}{\dot{n}_{EtOH,i} - \dot{n}_{EtOH,f}} \quad (2)$$

$$TOF = \frac{\dot{n}_{EtOH} * C * N_A}{m_{cat} * L_V * S_{BET}} \quad (3)$$

2.15. Anaerobic Titration. The anaerobic titration of VO_x using ethanol as a reductant was carried out using the reactor setup described above. To maintain an oxygen-free atmosphere, the reaction cell containing the catalyst sample was purged with N_2 overnight (46 mL/min) at a temperature of 190°C. Subsequently, ethanol was added to the feed (1.1%). Based on the results of the quantitative gas-phase analysis, the amount of redox active VO_x species can be determined by assuming that active V^{5+} species were irreversibly reduced to V^{3+} during anaerobic titration, each yielding one molecule of acetaldehyde. Please note that a reduction from V^{5+} to V^{3+} species during ODH of ethanol was postulated by Beck et al. and Kilos et al. [1,9]

3. Results and Discussion

3.1. Catalyst Preparation. As the synthesis of embedded VO_x catalysts is based on the ALD of metal oxides, the functional groups on the surface of GO are crucial for this approach. When the method for synthesizing GO described in the experimental section is applied, various carbon-oxygen species like hydroxyls, carbonyls, carboxyls, ethers, and epoxides are obtained. For the spectroscopic identification of these groups FTIR and XPS were employed (see Figure S1).

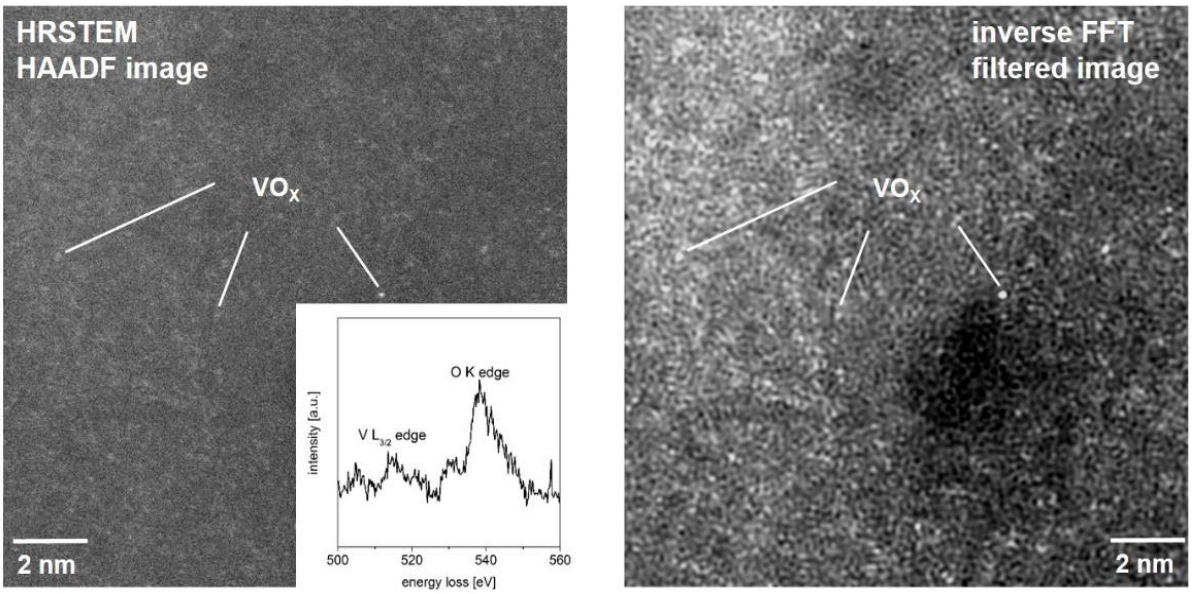

Figure 2. Left: HRSTEM HAADF image of GO ALD-coated with one cycle of VO_x. The inset shows an EEL spectrum of the region evidencing the presence of VO_x on the surface of GO. **Right:** Inverse FFT filtered representation of the image shown on the left.

The specific surface area of the as-synthesized GO was 80 m^2/g, as determined by N_2 physisorption experiments employing the standard BET analysis method. For the synthesis of embedded VO_x catalysts, VO_x was dispersed on GO using ALD (one cycle, exposure ≈ 24 × 10^6 L) in a first step. The dispersion of VO_x was monitored using HRSTEM. Figure 2 provides a high-angle annular dark field (HAADF) image of dispersed VO_x on GO (left) as well as the inverse fast Fourier transform (FFT) filtered representation (right). On the dark background of

the HAADF image distinct bright spots can be observed. Based on the characteristic V $L_{3/2}$ edge at 515 eV in the EEL spectrum (see inset), the assignment of the bright spots to small VO_x clusters appears plausible.[39,40] The inverse FFT filtered representation indicates, that in addition two-dimensional VO_x networks may be present on the GO surface, as can be seen in particular in the upper left corner. However, the size of the isolated VO_x clusters is far below 1 nm, and evidence for large V_2O_5 clusters could not be found. In contrast, on bare GO there was no indication of the presence of VO_x from HAADF or EEL spectra (not shown). Accordingly, we assign the observed features in Figure 2 to small, well-dispersed VO_x clusters on the surface of GO.

As the next step towards embedded VO_x catalysts, the VO_x species supported on GO were further ALD-coated and thus conserved within different metal oxide matrices (see Figure 1). The successful deposition of the Al_2O_3, SiO_2 and TiO_2 films was confirmed by XPS measurements. In Figure 3 the XP survey spectra of pure GO and GO coated with 10 nm of Al_2O_3, SiO_2, and TiO_2 are shown (on the left), besides detailed spectra of the corresponding O 1s regions (on the right). As expected, the spectrum of GO exhibits photoemissions from C 1s and O 1s core levels only.[37] Based on the results of the peak-fit analysis the surface elemental concentrations of C and O were calculated as 64.4 and 35.6 at.-%, respectively. Upon deposition of 10 nm SiO_2 (56 cycles) additional Si 2p and 2s emissions were observed at binding energies of 103.3 and 154.5 eV, respectively. The as-determined atomic ratio O:Si was 2 (Si = 28.2 at.-%, O = 56.3 at.-%), in agreement with the stoichiometry of SiO_2. The analysis of XP spectra obtained from Al_2O_3 and TiO_2 coated GO yields similar results. The ratio O:Al was determined as 1.6 and matches very well with the stoichiometry of Al_2O_3. Upon deposition of TiO_2 additional water was found on the surface of TiO_2-coated GO, presumably due to an increased surface hydrophilicity. When considering O 1s emissions from adsorbed water, the ratio O:Ti reduces from 2.8 to 2.1, in agreement to the stoichiometry of TiO_2. Detailed spectra of the O 1s regions in the left panel of Figure 3 show that the emissions of pure GO at 527.7, 528.8 and

529.8 eV completely vanish upon deposition of Al_2O_3, SiO_2 and TiO_2. New signals arising at 532.7, 531.3 and 530.7 eV can be attributed to O 1s emissions from SiO_2, Al_2O_3, and TiO_2, respectively,[37] thus strongly indicating that the oxide layer thickness exceeds the information depth of XPS, and that the deposited metal oxides form conformal layers. It should be mentioned that an additional contribution of C 1s emissions was detected in the spectra of the coated materials. However, based on detailed C 1s spectra (not shown) we can attribute the observed C 1s emissions to the presence of ubiquitous carbon.

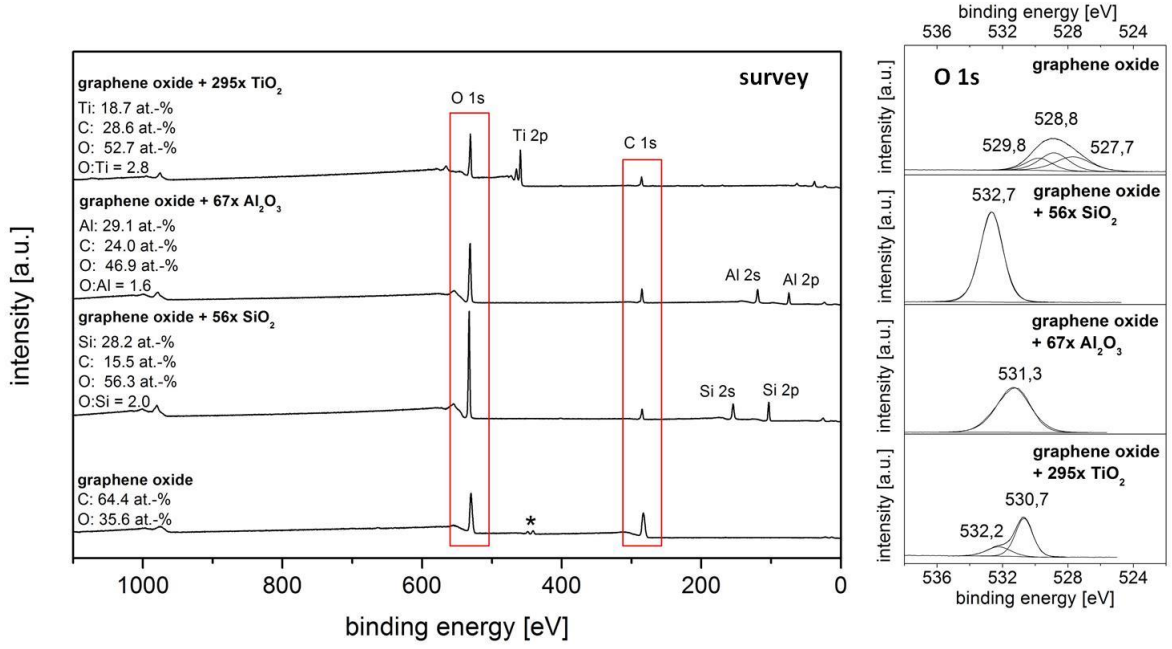

Figure 3. XP spectra of GO before and after the deposition of 10 nm SiO_2 (56 cycles), Al_2O_3 (67 cycles), and TiO_2 (295 cycles) using ALD. **Left:** The surface elemental concentrations in at.-% and the atomic ratios O:M (M = Al, Si, Ti) were calculated on the basis of the results from the peak-fit analysis. The signal marked with an asterisk in the spectrum of GO arises from photoelectron emissions from an indium foil used as a sample holder during the XPS measurements. **Right:** Corresponding high-resolution O 1s spectra, including the results from the peak-fit analysis.

As last step, the sacrificial GO support needs to be removed. To gain insight into the mechanism of template removal, the thermal decomposition of GO was investigated by TGA. Exemplarily, we will discuss the Al_2O_3-related data in the following (see Figure 4). To this end, three different types of samples consisting of GO, Al_2O_3, and VO_x were prepared: 1) GO coated with 67 ALD cycles of Al_2O_3 ("GO + 67×Al_2O_3"), 2a) GO coated with 67 ALD cycles of Al_2O_3 and then coated with 3 ALD cycles of VO_x ("GO + 3×VO_x-on-Al_2O_3"), 2b) GO coated with 67 ALD cycles of Al_2O_3 and then 10 ALD cycles of VO_x ("GO + 10×VO_x-on-Al_2O_3"), 3a) GO coated with 3 ALD cycles of VO_x and then 67 ALD cycles of Al_2O_3 ("GO + 3×VO_x-in-Al_2O_3"), and 3b) GO coated with 10 ALD cycles of VO_x and then 67 ALD cycles of Al_2O_3 ("GO + 10×VO_x-in-Al_2O_3"). Figure 4 compares the thermal decomposition of these ALD-coated GO samples to that of pure GO. The observed thermal decomposition of GO can be subdivided into four main sections: i) evaporation of water intercalated between the GO sheets, ii) degradation of less stable oxygen species (carboxyls, anhydrides, or lactones), iii) degradation of more stable oxygen species (hydroxyls and carbonyls), and iv) decomposition of the carbonaceous framework above 400°C.[37,41,42]

For pure GO (black curve) evaporation of water is observed up to 150°C and causes a weight loss of approximately 10%. The residual upon calcination of GO is <1%, confirming its high purity. The curves of the ALD-coated GO samples do not exhibit a weight loss in the first temperature range. Most likely the evaporation of water is hindered by the ALD metal oxide films. Above 180°C a mass loss related to the decomposition of less stable species is observed in all TGA curves. The presence of the ALD layers does not seem to affect this process, furthermore implying that the less stable species do not serve as functional groups during the ALD process. Subsequently, the curves of GO and GO + 67× Al_2O_3 run almost parallel with a slight shift towards higher temperatures for GO + 67× Al_2O_3. The deposition of VO_x preceding the Al_2O_3 coating reduces the temperature necessary for the decomposition of the carbonaceous

framework from 400 to approximately 300°C. This effect is attributed to the catalytic properties of VO_x enabling the decomposition of the carbon matrix at lower temperatures. We propose that the decomposition take places at the GO/VO_x-interphase, consistent with Figure 1, which shows that VO_x is not encapsulated but rather embedded in the Al_2O_3 layer. Comparison of the dotted and dashed blue curves implies, that the amount of VO_x influence neither the rate of decomposition nor the temperature necessary for the decomposition. Owing to the missing GO/VO_x-interphase, we do not expect this behavior to be observed for GO + 3×VO_x-on-Al_2O_3 and GO + 10×VO_x-on-Al_2O_3. This is confirmed by the dotted and dashed black TGA curves, resembling the decomposition curve of GO + 67× Al_2O_3. The residual of all ALD coated samples is approximately 5%.

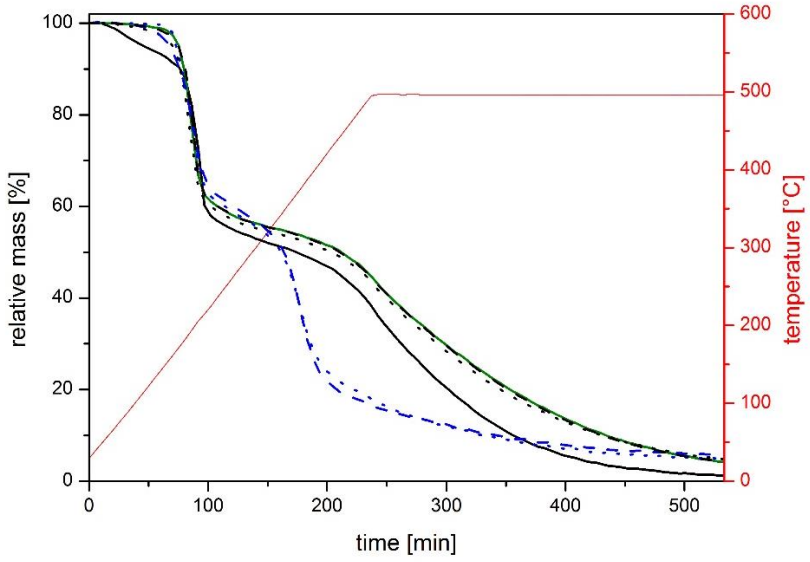

Figure 4. TGA curves showing the thermal decomposition of different GO samples. Black curve: GO. Green curve: GO + 67× Al_2O_3. Dotted black curve: GO + 3×VO_x-on-Al_2O_3. Dashed black curve: GO + 10×VO_x-on-Al_2O_3. Dotted blue curve: GO + 3×VO_x-in-Al_2O_3. Dashed blue curve: GO + 10×VO_x-in-Al_2O_3. The red graph displays the temperature.

Using a combination of physical characterization (N_2 physisorption) and ICP-OES, the VO_x loadings L_V of the embedded VO_x catalysts were calculated. Since all samples were treated equally before the thermal treatment, one would expect that all catalysts should have similar specific surface areas and VO_x loadings. The results are summarized in Table 3. According to the results of the BET analysis, the calcined samples exhibit considerably larger specific surface areas than the ozonolyzed samples. While the specific surface area of the ozonolyzed samples is almost equal (32–34 m^2/g), the specific surface area of 1×VO_x-in-SiO_2-calc. (124 m^2/g) is considerably larger than those of the other calcined samples 1×VO_x-in-Al_2O_3-calc. and 1×VO_x-in-TiO_2-calc. (74 m^2/g). Despite the lower specific surface area of the calcined samples, the VO_x loadings of these catalysts are noticeable higher than those of the ozonolyzed samples (factor 1.3–1.8). In each case, the loading (14.3–22.5 V/nm^2) is far above the theoretical monolayer coverage of 8 V/nm^2 for dispersed VO_x supported on Al_2O_3 and TiO_2 and 2.6 V/nm^2 for dispersed VO_x supported on SiO_2.[5,14,43,44] In this context the catalyst 1×VO_x-in-TiO_2-ozone represents the only exception, revealing a VO_x loading near monolayer coverage (8 V/nm^2).[43] Thus, the analysis indicates that the thermal treatment for removing the GO has a significant influence on both, specific surface area and VO_x loading, and thus on the structure of the catalyst. Based on these findings, one may assume that the initial VO_x dispersion (see Table 3) is at least partially converted into three-dimensional VO_x structures and thus probably into crystalline V_2O_5 during thermal treatment. On the other hand, the embedding of VO_x species in a supporting metal oxide matrix may allow a higher dispersion and thus higher loadings without the formation of V_2O_5 crystallites.

3.2. Catalyst Characterization. The molecular structure of the embedded VO_x species was studied by Raman and UV-vis spectroscopy. The UV Raman, visible Raman, and UV-vis spectra of the catalysts listed in Table 3 are shown in Figures 5–8 and will be discussed separately for each ‘support’ material (Al_2O_3, SiO_2, TiO_2) in the following.

Table 3. BET surface area (S_{BET}), vanadium loading (L_V) and corrected vanadium loadings $L_{V,corr}$ based on the results of the anaerobic titration of the embedded VO_x catalysts.

Sample	S_{BET} [m^2/g]	L_V [V/nm^2]	$L_{V,corr}$ [V/nm^2]
1×VO_x-in-Al_2O_3-calc.	74	22.5	17
1×VO_x-in-Al_2O_3-ozone	32	17.7	8
1×VO_x-in-SiO_2-calc.	124	22.2	15
1×VO_x-in-SiO_2-ozone	34	16.6	9
1×VO_x-in-TiO_2-calc.	74	14.3	-
1×VO_x-in-TiO_2-ozone	34	8.0	-

Raman spectra of the catalysts 1×VO_x-in-Al_2O_3 prepared by a) calcination and b) thermal ozone treatment are depicted in Figure 5. The UV Raman spectrum of the catalyst 1×VO_x-in-Al_2O_3-calc. is dominated by a broad asymmetric band between 750 and 1025 cm^{-1} showing a maximum at 960 cm^{-1} and a shoulder at around 1020 cm^{-1}. These features can be assigned to Al–O–V interphase vibrations and V=O stretching vibrations of dispersed VO_x, respectively.[10,11,19,45,46] In particular, the existence of an Al–O–V interphase band confirms the successful formation of a covalent Al–O–V interphase bond during the catalyst's synthesis. This bond is crucial for the stability of the embedded VO_x species. A weaker band is observed at 520 cm^{-1} and indicates the presence of oligomeric VO_x.[19,45] Bands located at higher wavenumbers, i.e., at 1390, 1544 and 1590 cm^{-1}, are not related to VO_x vibrations, but rather originate from residual carbon, namely the D and G bands at 1390 and 1590 cm^{-1}, as well as gas-phase oxygen (1544 cm^{-1}).[37,41,47] The visible Raman spectrum of this sample shows merely one band at 460 cm^{-1}, which can be assigned to V–O–V vibrations of oligomeric VO_x.[16,45] Please note that visible Raman spectra were recorded from 'as is' samples, i.e., under ambient conditions. It is known that during hydration the molecular structure of VO_x changes and the

characteristic V=O band may not be observed anymore.[19] Considering the low intensity of the V-O-V band observed at 460 cm^{-1}, it is therefore reasonable to assume that the absence of a distinct V=O band is related to the presence of moisture on the catalyst's surface. Despite the high VO_x loading (see Table 3) and the ~10-fold higher Raman scattering cross-section of crystalline V_2O_5 compared to dispersed VO_x for 514 nm Raman excitation, the characteristic sharp V_2O_5 bands were not observed.[46] We can thus exclude the presence of V_2O_5 microcrystallites on the catalyst surface. To explain the high VO_x loading far above monolayer coverage (see Table 3) it is plausible to assume crystalline V_2O_5 nanoparticles, which due to their size are not detected by visible Raman spectroscopy or, alternatively, amorphous three-dimensional VO_x species. The corresponding UV-vis spectrum of this catalyst is shown in Figure 8 a). The spectrum is characterized by major absorption between 200 and 400 nm with a maximum at 270 nm and an additional shoulder at 400–550 nm. In contrast, the spectrum of the bare Al_2O_3 support (see Figure 8 c)) does not show significant absorption in this region. The intense UV absorption at 270 nm may be assigned to monomeric VO_4 and short-chain oligomeric VO_x species, thus indicating the presence of highly dispersed VO_x species. Absorption at longer wavelengths additionally suggests the presence of small amounts of long-chain oligomeric VO_x or even crystalline V_2O_5.[12,15,19,48] However, since no evidence for crystalline V_2O_5 was found in the visible Raman spectrum, the shoulder at 400 nm is attributed to long-chain oligomeric VO_x. We thus conclude, that the high dispersion achieved by VO_x ALD was sustained during Al_2O_3 ALD and template removal using calcination.

The UV Raman spectrum recorded from the catalyst 1×VO_x-in-Al_2O_3-ozone exhibits a very poor signal-to-noise ratio, which may result from the lower specific surface area of the catalyst or residual carbon due to the incomplete decomposition of GO. As a consequence, Raman bands cannot be clearly identified for UV excitation. In contrast, the signal-to-noise ratio of the visible Raman spectrum is not affected by this effect. Besides the band at 460 cm^{-1} assigned to V–O–

V vibrations of oligomeric VO_x, which was also observed in the visible Raman spectrum of the catalyst $1\times VO_x$-in-Al_2O_3-calc., there is another Raman feature with two apparent maxima at 700 and 800 cm^{-1}. With respect to the noticeable lower specific surface area of the catalyst $1\times VO_x$-in-Al_2O_3-ozone compared to the catalyst $1\times VO_x$-in-Al_2O_3-calc. (see Table 3), thermal ozone treatment might induce extensive oligomerization of the originally well dispersed VO_x. Since Raman shifts of V–O–V vibrations are typically found between 400 and 800 cm^{-1} we assume the bands at 700 and 800 cm^{-1} to be related to V–O–V vibrations of VO_x species with a higher degree of oligomerization.[15] Additional evidence for this suggestion is provided by the corresponding UV-vis spectrum shown in Figure 8 b). Compared to the calcined catalyst, absorption at 270 nm is much lower in the spectrum of the ozonolyzed catalyst and a second maximum was observed at around 400 nm. These findings indicate that the catalyst $1\times VO_x$-in-Al_2O_3-ozone indeed bears a higher content of long-chain oligomeric VO_x, while no evidence for crystalline V_2O_5 was found, fully consistent with the Raman data.

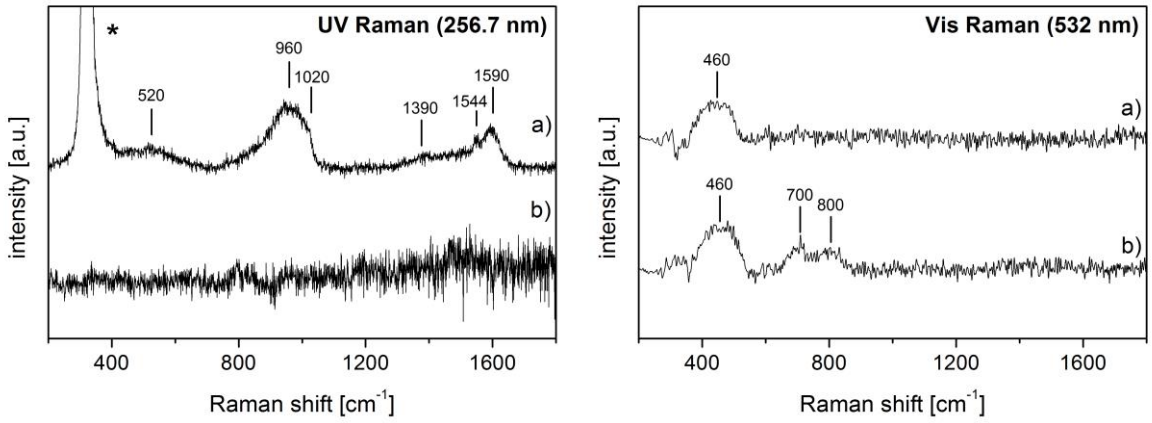

Figure 5. UV (left) and visible (right) Raman spectra of the catalysts a) $1\times VO_x$-in-Al_2O_3-calc. and b) $1\times VO_x$-in-Al_2O_3-ozone. Spectra are offset for clarity. The band marked with an asterisk is a feature arising from the CaF_2 window of the reaction cell.

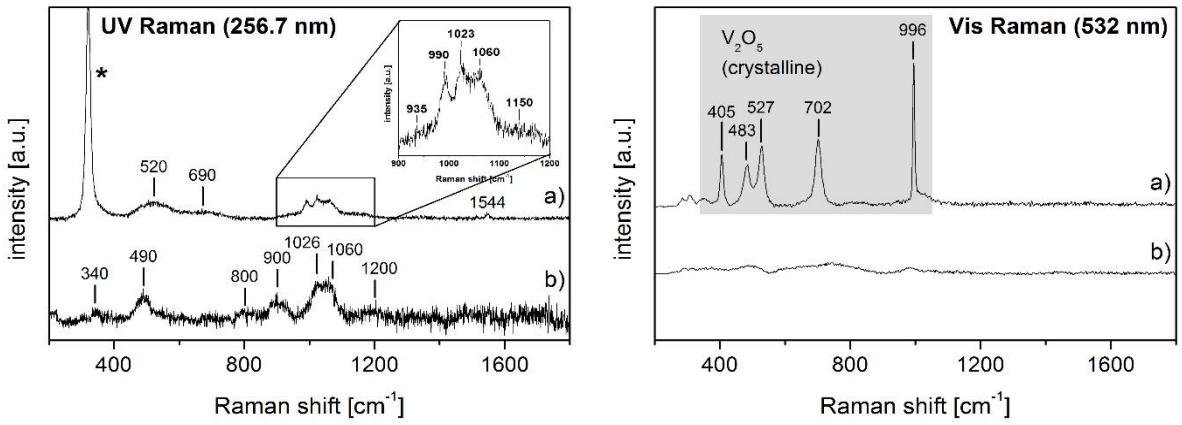

Figure 6. UV (left) and Vis (right) Raman spectra of the catalysts a) 1×VO_x-in-SiO_2-calc. and b) 1×VO_x-in-SiO_2-ozone. Spectra are offset for clarity. The inset in the left panel provides an enlarged view of the region between 900 and 1200 cm^{-1}. The shaded area in the right panel highlights the Raman bands arising from crystalline V_2O_5. The band marked with an asterisk is a feature arising from the CaF_2 window of the reaction cell.

In Figure 6 UV and visible Raman spectra of VO_x embedded in SiO_2 are shown for a) calcined and b) ozonolyzed samples. The UV Raman spectrum of the catalyst 1×VO_x-in-SiO_2-calc. exhibits bands at 520, 690, 935, 990, 1023, 1060, 1150, and 1544 cm^{-1} (see inset). These bands can be assigned to different types of V–O vibrations, i.e., vanadyl V=O, interphase Si–O–V, and oligomeric V–O–V vibrations, as well as gas-phase oxygen (band at 1544 cm^{-1}).[6,12,16,47,48] While the bands at 520 and 690 cm^{-1} are located in the region typical of V–O–V vibrations, the band at 1150 cm^{-1} may represent a combination or overtone vibration of these V–O–V vibrations.[16] The bands at 935 and 1060 cm^{-1} can be assigned to in and out of phase Si–O–V vibrations, respectively, thus confirming the successful interphase formation of a covalent Si–O–V bond (see above).[16] Furthermore, two types of V=O stretching vibrations, located at 990 and 1023 cm^{-1}, were found in the spectrum, strongly indicating the presence of both, dispersed VO_x and crystalline V_2O_5.[6,12,16,48] In agreement, the visible Raman spectrum of this catalyst shows the characteristic sharp bands of V_2O_5 at 405, 483, 527, 702, and 996 cm^{-1}.[14]

Accordingly, the UV-vis spectrum (see Figure 8 d)) shows broad absorption between 200 and 550 nm with two maxima at 270 and at around 370 nm, indicating a mixture of isolated VO_4, short, and long-chain oligomeric VO_x, and possibly crystalline V_2O_5.[12,15,19,48] Absorption of the bare SiO_2 support is negligible (see spectrum f)). Considering the similar VO_x loading of the two catalysts 1×VO_x-in-Al_2O_3-calc. and 1×VO_x-in-SiO_2-calc. (see Table 3), it is noticeable that crystalline V_2O_5 was evidenced only on the SiO_2 support. We attribute this behavior to the preferred crystallization of VO_x on SiO_2 owing to the lower bond strength of Si–O–V as compared to Al–O–V.[11,23,24]

Turning to the ozonolyzed catalyst 1×VO_x-in-SiO_2-ozone, we find the signal-to-noise ratio of the UV Raman spectrum again much lower, most likely owing to its smaller specific surface area (see Table 3) or residual carbon. Still, several bands were observed at 340, 490, 800, 900, 1026, 1060, and 1200 cm^{-1}, in contrast to the UV Raman spectrum of the catalyst 1×VO_x-in-Al_2O_3-ozone with a similar specific surface area. Bands at 490 and 800 cm^{-1} may be attributed to V–O–V vibrations of oligomeric VO_x.[16] The band at 1200 cm^{-1} may present an overtone or a combination band of these V–O–V vibrations. Besides, V=O stretching and bending modes were observed at 340 and 1026 cm^{-1}, respectively, indicating the presence of well dispersed VO_4. Bands at 900 and 1060 cm^{-1} can be assigned to in and out of phase Si–O–V interphase vibrations.[12,16,49] Please note that neither the UV nor the visible Raman spectrum suggest the presence of crystalline V_2O_5. The visible Raman spectrum merely shows broad bands with low intensity at around 485, 730, and 980 cm^{-1}, which may indicate V–O–V and Si–OH vibrations.[12,16] Thus, despite the small specific surface area and the high loading (see Table 3), no evidence for crystalline V_2O_5 could be found. Additionally, the broad absorption between 200 and 550 nm in the UV-vis spectrum in Figure 8 e) confirms the presence of dispersed monomeric and oligomeric VO_x.[19] As in the case of VO_x embedded in Al_2O_3, embedding VO_x in SiO_2 also yields an M–O–V (M = Al, Si) interphase that is crucial for the catalyst stability.

Furthermore, the results indicate that the nature of thermal treatment strongly affects the catalyst structure on the microscopic scale. While calcination yields a larger specific surface area and the presence of crystalline V_2O_5 on a SiO_2 support, thermal ozone treatment yields a smaller specific surface area but dispersed VO_x.

The UV Raman spectroscopic investigation of the catalysts 1×VO_x-in-TiO_2-calc. and 1×VO_x-in-TiO_2-ozone is challenging owing to the strong absorption of the supporting TiO_2 in the UV range (see Figure 8 i)). In the UV Raman spectrum obtained from the catalyst 1×VO_x-in-TiO_2-calc. (see Figure 7 a), left) solely two bands were observed at 1354 and 1544 cm^{-1}, originating from boron nitride, which was used to focus the laser and gas-phase oxygen, respectively.[47,50] The visible Raman spectrum on the other hand gives rise to three sharp bands at 397, 515, and 640 cm^{-1}, which can readily be assigned to crystalline TiO_2 (anatase).[34] We thus believe, that calcination of the initially amorphous TiO_2 ALD layers yields at least partial crystallization of the TiO_2 support. In addition, a band was observed at around 807 cm^{-1}, which indicates V–O–V vibrations and thus the presence of oligomeric VO_x.[34] The two sharp bands at 397 and 515 cm^{-1} may overlap with a V–O–V band at 460 cm^{-1}, that has been observed in all visible Raman spectra so far (see above).

The UV and visible Raman spectra of the catalyst 1×VO_x-in-TiO_2-ozone are shown in Figure 7 b). As observed for all ozonolyzed catalysts, the signal-to-noise ratio is poor for the UV Raman spectrum and thus only two weak bands were observed at 344 and 623 cm^{-1}. While the band at 623 cm^{-1} lies within the range of V–O–V vibrations, the band at 344 cm^{-1} may be assigned to a V=O bending mode.[16] However, this assignment is questionable, since no corresponding V=O stretching band (>1000 cm^{-1}) was observed. Using visible Raman excitation, V–O–V vibrational bands were observed, at 460 and 807 cm^{-1}, that were also found in the visible Raman spectrum of the catalyst 1×VO_x-in-TiO_2-calc. (see above). Additionally, a weak band appears at 608 cm^{-1}, which may also represent V–O–V vibrations of oligomeric VO_x.[16] It is possible

that this band was not observable in the visible Raman spectrum of the catalyst 1×VO_x-in-TiO_2-calc. due to its low intensity and an overlap with the sharp band at 640 cm^{-1}.

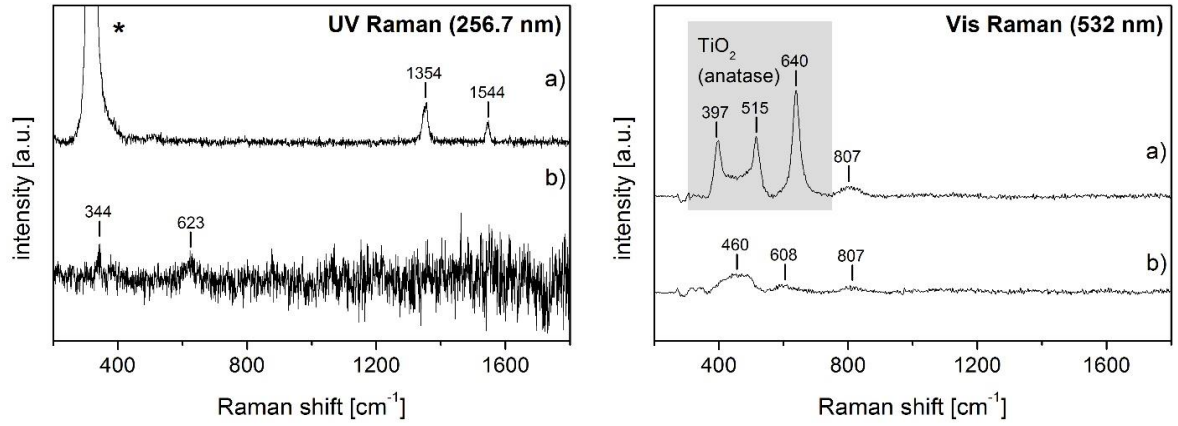

Figure 7. UV (left) and visible (right) Raman spectra of the catalysts a) 1×VO_x-in-TiO_2-calc. and b) 1×VO_x-in-TiO_2-ozone. Spectra are offset for clarity. The shaded area highlights the Raman bands arising from crystalline TiO_2 (anatase). The band marked with an asterisk is a feature arising from the CaF_2 window of the reaction cell.

The UV-vis spectra of the TiO_2 embedded VO_x catalysts are shown in Figure 8 g) and h). Both spectra exhibit strong absorption between 200 and 400 nm and a shoulder at 400–600 nm. Since no evidence for crystalline V_2O_5 was found in the visible Raman spectra, the absorption at 400–600 nm may be attributed to highly oligomerized VO_x. An explicit assignment of the absorption between 200 and 400 nm to monomeric VO_4 and short-chain oligomeric VO_x is difficult due to an overlap with the strong absorption of the supporting TiO_2 (see spectrum i)). Nevertheless, the spectrum of the catalyst 1×VO_x-in-TiO_2-calc. exhibits an absorption maximum at 330 nm and two shoulders at shorter wavelength at 310 and 270 nm, indicating the presence of monomeric and oligomeric VO_x species.[19] The spectrum of the catalyst 1×VO_x-in-TiO_2-ozone shows weaker absorption between 200 and 400 nm than the TiO_2 support, but the shape of the absorption band clearly differs. While the catalyst 1×VO_x-in-TiO_2-ozone exhibits an absorption

maximum at 270 nm and a shoulder at 310 nm (see spectrum h)), the spectrum of the TiO_2 support (see spectrum i)) shows two maxima of almost equal intensity. Thus, the presence of monomeric and oligomeric VO_x is suggested.[19] Unlike the spectroscopic analysis of VO_x embedded in Al_2O_3 and SiO_2, the UV and Raman spectroscopic investigation of VO_x embedded in TiO_2 yields only limited information due to absorption effects of the supporting TiO_2. Therefore, it was not possible to confirm the successful formation of a covalent Ti–O–V interphase bond in this case. Still, spectroscopic evidence was found that VO_x was present as well-dispersed species. Furthermore, the thermal treatment significantly affected the chemical nature of the TiO_2 support by yielding anatase TiO_2 upon calcination and amorphous TiO_2 upon ozone treatment.

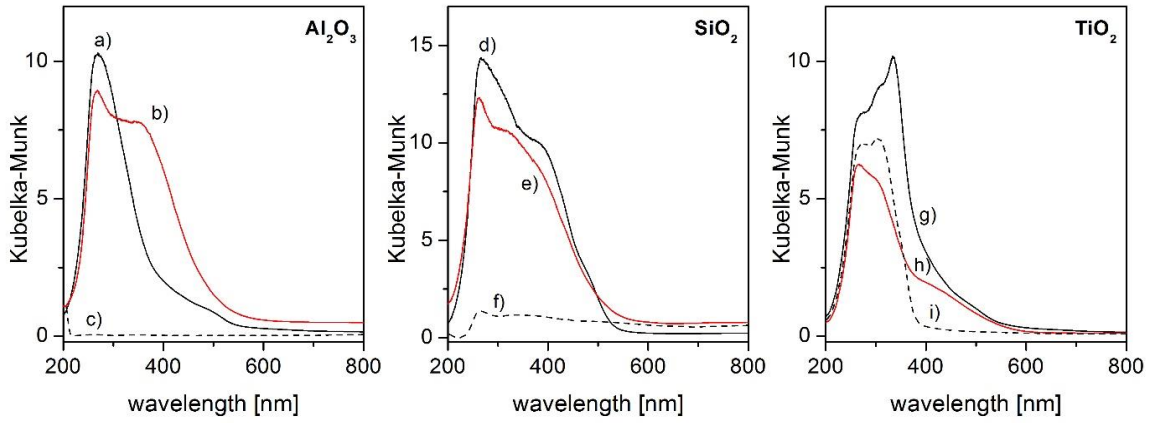

Figure 8. UV-vis spectra of the catalysts a) 1×VO_x-in-Al_2O_3-calc., b) 1×VO_x-in-Al_2O_3-ozone, d) 1×VO_x-in-SiO_2-calc., e) 1×VO_x-in-SiO_2-ozone, g) 1×VO_x-in-TiO_2-calc., and h) 1×VO_x-in-TiO_2-ozone. For better visualization the spectra recorded from the ozonolyzed catalysts are plotted in red. The UV-vis spectra of the corresponding supporting materials Al_2O_3, SiO_2, and TiO_2 are shown as dashed lines c), f), and i), respectively.

3.3. Structural Models. To gain insight into the molecular structure of the embedded VO_x catalysts, detailed spectroscopic characterization was carried out as described in the previous section. Combining these results with the findings from the BET and ICP-OES analysis allows us to propose two possible structures for the embedded VO_x catalysts shown schematically in Figure 9. These need to take into account that according to the ICP-OES analysis, the VO_X loading of all catalysts was significantly above monolayer coverage, but evidence for crystalline V_2O_5 was not found except for 1×VO_x-in-SiO_2-calc.

On the one hand, it is possible that during thermal treatment sintering of metal oxide particles (Al_2O_3, SiO_2, TiO_2) occurred and that some VO_x species were encapsulated within the bulk material of the supporting matrix (see Figure 9, left). Porous structures in the metal oxide matrix may facilitate the accessibility of active sites to reactants during heterogeneous catalysis. However, one may expect the apparent VO_x loading to overestimate the real loading of accessible VO_x species relevant to catalysis. In fact, quantification of the number of accessible redox active vanadium sites by titration with ethanol under anaerobic conditions (see Experimental Section) yields the corrected lower vanadium loadings ($L_{V,corr}$) given in Table 3. Please note that for the catalysts 1×VO_x-in-TiO_2-calc. and 1×VO_x-in-TiO_2-ozone the titration did not yield reasonable results because the titration was adulterated by simultaneous reduction of Ti^{4+}. On the other hand, to explain the high loadings without the presence of a distinct crystalline phase, we cannot exclude the formation of three-dimensional structures such as i) crystalline V_2O_5 nanoparticles, which is not detectable by visible Raman spectroscopy owing to its small size, or ii) multilayered amorphous VO_x (see Figure 9, right).

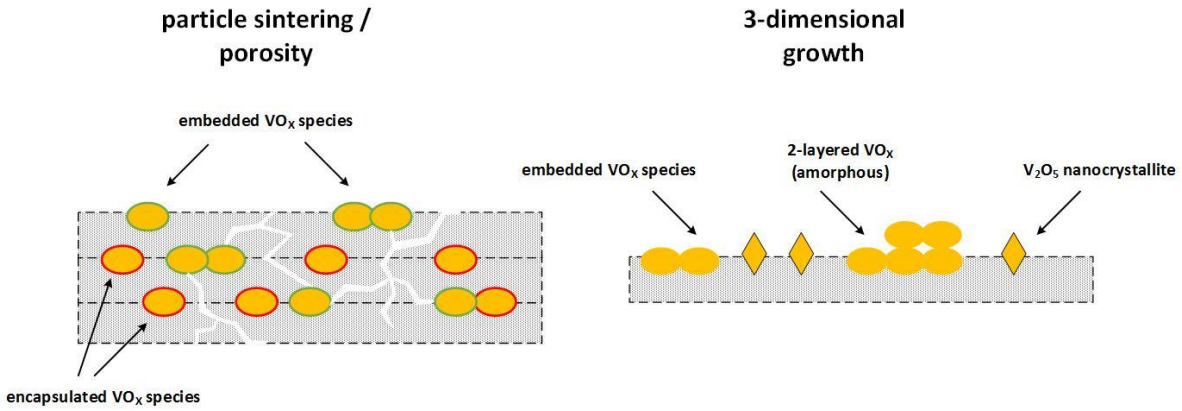

Figure 9. Proposed structures for the VO_x catalysts prepared by ALD assisted synthesis, consisting of embedded and encapsulated VO_x species as well as possibly three-dimensional amorphous and/or crystalline species.

3.4. Catalytic Performance. The catalytic relevance of the embedded VO_x structures was demonstrated in the ODH of ethanol. For comparison with literature data TOF values were calculated based on the corrected vanadium loadings $L_{V,corr}$ (see Table 3). Table 4 compares catalytic results from our experiments with data from the literature.[1,7,9,15,51-53] Our results indicate that the conversion and selectivity of the embedded catalysts is influenced most strongly by the type of template removal, and to a lower extent by the supporting metal oxide. Despite their lower VO_x loadings the ozonolyzed catalysts exhibited higher conversion rates than the calcined catalysts. As a consequence, the TOF values for ozonolyzed VO_x embedded in Al_2O_3 and SiO_2 were at least one order of magnitude higher than those for the calcined catalysts. This effect is significantly weaker in the case of VO_x embedded in TiO_2 (factor of 2) and may either be related to exceptionally strong catalyst-support interactions or the presence of crystalline TiO_2 (see Figure 7) after calcination.

The reported TOF values for Al_2O_3-supported VO_x lie between 0.6 and 7.9×10^{-3} s^{-1}. Thus, the TOF value for $1\times VO_x$-in-Al_2O_3-calc. (1.7×10^{-3} s^{-1}) is located in the lower region of the reported values, while that of $1\times VO_x$-in-Al_2O_3-ozone (20.93×10^{-3} s^{-1}) is at least one order of magnitude higher than the reported activities. With respect to the selectivity towards acetaldehyde, the performance of the ozonolyzed catalyst is comparable to the literature data for supported VO_x catalysts; in contrast, the calcined catalyst provides the highest selectivity, 95%, among the VO_x-Al_2O_3 catalysts.

The TOF values for $1\times VO_x$-in-TiO_2-calc. and $1\times VO_x$-in-TiO_2-ozone are 4.14×10^{-3} s^{-1} and 8.49×10^{-3} s^{-1}, respectively, and thus approximately one to two orders of magnitude below the TOF reported in the literature for VO_x/TiO_2 catalysts tested at similar temperatures. In this context it should be mentioned, that the TiO_2-supported catalysts described in the literature consisted of crystalline TiO_2 (mainly anatase), while the TiO_2 present in our catalysts was completely amorphous for the ozonolyzed samples and only partially crystalline for the calcined samples. To investigate the structural, electronic, and optical properties of amorphous and

crystalline TiO_2 (anatase), Prasai et al. employed density functional theory (DFT) calculations but found that they were rather similar.[54] Thus, catalyst-support interactions arising from different phases of the TiO_2 support may be negligible. In a very recent study, Samek et al. reported on the reducibility of VO_x supported on amorphous TiO_2 (grown by ALD) and on anatase.[55] In agreement with the aforementioned, they found that the reducibility, which is considered as a descriptor for the redox activity of supported VO_x, was comparable for the two TiO_2 phases. With respect to the influence of the VO_x loading, Yun et al. found a positive correlation between the VO_x loading and the defect formation enthalpy for oxygen vacancies, which inversely scales with the reducibility of the VO_x species.[53] Thus, the higher TOF values for VO_x supported on TiO_2, reported in the literature, may be related to different V_x loadings rather than to different phases of TiO_2.

For VO_x embedded in SiO_2 our catalysts yielded TOF values of 0.65×10^{-3} s^{-1} (calc.) and 8.37×10^{-3} s^{-1} (ozone), which are comparable to the values of VO_x embedded in Al_2O_3 and TiO_2 (see above). Since the literature does not provide much data for the catalytic ODH of ethanol for VO_x supported on SiO_2, it is more difficult to properly rank these results. However, the role of the oxide support on the catalytic activity has been studied extensively for other catalytic reactions.[1,56] For the partial oxidation of methanol it was found that the activity of supported VO_x catalysts follows the ranking $VO_x/TiO_2 >> VO_x/Al_2O_3 > VO_x/SiO_2$.[56] This effect has been attributed to the inversely increasing electronegativity of the supporting oxides and thus, the higher electron density at the M–O–V (M = Al, Si, Ti) interphase band.[56] Besides, the dispersion of VO_x may play a major role in the activity of supported VO_x catalysts prepared by conventional methods. In fact, it is well-known that the use of Al_2O_3 and TiO_2 support materials facilitates a much higher dispersion of VO_x than SiO_2, since the theoretical monolayer coverage is approximately 8 V/nm^2 for Al_2O_3 and TiO_2 but only 2.6 for SiO_2.[5,4,43,44] Interestingly, our results indicate that the embedding approach enables a much higher loading and dispersion of VO_x on different oxide supports (Al_2O_3, SiO_2, TiO_2), and the TOF values for the ODH of

ethanol are comparable for all tested catalysts. As shown above, our approach allows the limit of the lower loadings of dispersed vanadia on silica to be overcome, thus significantly increasing the reactivity of VO_x/SiO_2 catalysts in ODH reactions.

Based on the data of the embedded VO_x catalysts and comparison with literature data, the embedded catalysts are found to present a promising class of oxide catalysts. While calcined catalysts provide a higher selectivity towards acetaldehyde, ozonolyzed catalysts exhibit significantly higher TOF values. In comparison to supported VO_x catalysts prepared by conventional synthesis methods, a distinct increase in activity was found for the VO_x species embedded in Al_2O_3 and SiO_2 after ozone treatment. In the case of the titania based systems, the TOF values were lower than reported in the literature, which may be related either to the VO_x loading or the partial pressure of ethanol rather than the crystallinity of the TiO_2 phase. It is worth mentioning that the calcined catalysts showed higher selectivities towards acetaldehyde than most of the supported catalysts, reaching up to 98%.

Table 4. Literature overview of the activities of supported VO_x catalysts in the ODH of ethanol to acetaldehyde. Given are the reaction temperature (T), the turnover frequency (TOF) and the selectivity towards acetaldehyde (S_{aca}). The catalytic results for catalysts discussed in this work are highlighted.

Catalyst	T [°C]	TOF [10^{-3} s^{-1}]	S_{aca} [%]	Reference
VO_x/Al_2O_3	200	6.00*	85	1
	200	7.90	80	9
	180	0.6*	67	52
	190	1.70[a]	95[a]	This work
	190	20.93[b]	87[b]	
VO_x/TiO_2	200	410.00*	>98	1
	180	21.70*	100	52
	150	3.60	68	51
	110	0.44	100	
	200	5.00	20	7
	120	0.75	90	
	200	100-1000	>99.5	53
	190	4.14[a]	98[a]	This work
	190	8.49[b]	72[b]	
VO_x/SiO_2	190	0.65[a]	87[a]	This work
	190	8.37[b]	57[b]	

[a] Calcined sample
[b] Ozonolyzed sample
*Referenced to ethanol conversion to acetaldehyde

4. Conclusions

An ALD-based approach allowing the fabrication of nanostructured embedded VO_x catalysts is presented, which aims to maximize the catalyst-support interactions for increased catalytic activity and sintering resistance. To this end, dispersed VO_x was temporarily supported on GO serving as a sacrificial template. The dispersion was embedded into a supporting metal oxide matrix (Al_2O_3, SiO_2, TiO_2) by applying ALD coatings. GO was then removed by thermal decomposition by either calcination or thermal ozone treatment. Based on thermogravimetric measurements it was shown that VO_x is not encapsulated by the supporting metal oxide but rather exhibits a solid/gas interphase that is crucial for catalytic activity. The initial dispersion of VO_x on GO was substantiated by combined TEM and EELS analysis.

Structural characterization of the final catalysts was carried out using multiple spectroscopic methods. The results indicate that despite the high loadings (L_V > monolayer coverage) VO_x was highly dispersed on Al_2O_3 and TiO_2. Although the loading of VO_x embedded in SiO_2 was comparable to that of VO_x embedded in Al_2O_3, template removal by calcination resulted in the presence of crystalline V_2O_5 on the SiO_2 support, while upon ozone treatment dispersed VO_x was obtained. For all the catalysts studied, calcination yielded significantly larger specific surface areas than did ozone treatment. Based on the findings from the physical and structural characterization as well as the results from the anaerobic titration, we propose a structural model for the embedded VO_x catalysts, while we cannot exclude the presence of multilayered amorphous VO_x or crystalline V_2O_5 nanoparticles. UV Raman spectra confirm the successful formation of a VO_x-support interphase, which is decisively involved in the postulated mechanisms for VO_x-catalyzed oxidative dehydrogenation (ODH) reactions.

The embedded vanadia catalysts are active in the ODH of ethanol. Moreover, the catalytic performance of this new class of vanadia catalysts compares favorably with literature data on

conventional supported vanadia catalysts, thus highlighting the feasibility of rational catalyst engineering for supported oxide catalysts.

Supporting Information

Structural characterization using IR and XP spectroscopy; supporting Figure.

Acknowledgments

The authors thank Karl Kopp for performing XPS experiments, Martin Brodrecht for BET analysis, Dr. Stefan Lauterbach and Prof. H.-J. Kleebe for TEM characterization, as well as Marcel Heber for assistance with the visible Raman spectrometer. Financial support by the Deutsche Forschungsgemeinschaft (DFG-FOR1583) is gratefully acknowledged.

References

1. Beck, B.; Harth, M.; Hamilton, N. G.; Carrero, C.; Uhlrich, J. J.; Trunschke, A.; Shaikhutdinov, S.; Schubert, H.; Freund, H. J.; Schlögl, R.; Sauer, J.; Schomäcker, R., Partial Oxidation of Ethanol on Vanadia Catalysts on Supporting Oxides With Different Redox Properties Compared to Propane. *J. Catal.* **2012,** *296*, 120-131.
2. Briand, L. E.; Tkachenko, O. P.; Guraya, M.; Gao, X. T.; Wachs, I. E.; Grunert, W., Surface-Analytical Studies of Supported Vanadium Oxide Monolayer Catalysts. *J. Phys. Chem. B* **2004,** *108*, 4823-4830.
3. Carrero, C. A.; Schloegl, R.; Wachs, I. E.; Schomaecker, R., Critical Literature Review of the Kinetics for the Oxidative Dehydrogenation of Propane over Well-Defined Supported Vanadium Oxide Catalysts. *ACS Catal.* **2014,** *4*, 3357-3380.
4. Chua, Y. T.; Stair, P. C.; Wachs, I. E., A Comparison of Ultraviolet and Visible Raman Spectra of Supported Metal Oxide Catalysts. *J. Phys. Chem. B* **2001,** *105*, 8600-8606.
5. Gao, X. T.; Bare, S. R.; Weckhuysen, B. M.; Wachs, I. E., In Situ Spectroscopic Investigation of Molecular Structures of Highly Dispersed Vanadium Oxide on Silica Under Various Conditions. *J. Phys. Chem. B* **1998,** *102*, 10842-10852.
6. Hess, C.; Hoefelmeyer, J. D.; Tilley, T. D., Spectroscopic Characterization of Highly Dispersed Vanadia Supported on SBA-15. *J. Phys. Chem. B* **2004,** *108*, 9703-9709.
7. Kaichev, V. V.; Chesalov, Y. A.; Saraev, A. A.; Klyushin, A. Y.; Knop-Gericke, A.; Andrushkevich, T. V.; Bukhtiyarov, V. I., Redox Mechanism for Selective Oxidation of Ethanol Over Monolayer V_2O_5/TiO_2 Catalysts. *J. Catal.* **2016,** *338*, 82-93.
8. Khodakov, A.; Olthof, B.; Bell, A. T.; Iglesia, E., Structure and Catalytic Properties of Supported Vanadium Oxides: Support Effects on Oxidative Dehydrogenation Reactions. *J. Catal.* **1999,** *181*, 205-216.
9. Kilos, B.; Bell, A. T.; Iglesia, E., Mechanism and Site Requirements for Ethanol Oxidation on Vanadium Oxide Domains. *J. Phys. Chem. C* **2009,** *113*, 2830-2836.
10. Kim, H.; Ferguson, G. A.; Cheng, L.; Zygmunt, S. A.; Stair, P. C.; Curtiss, L. A., Structure-Specific Reactivity of Alumina-Supported Monomeric Vanadium Oxide Species. *J. Phys. Chem. C* **2012,** *116*, 2927-2932.
11. Magg, N.; Immaraporn, B.; Giorgi, J. B.; Schroeder, T.; Bäumer, M.; Döbler, J.; Wu, Z.; Kondratenko, E.; Cherian, M.; Baerns, M.; Stair, P. C.; Sauer, J.; Freund, H.-J., Vibrational Spectra of Alumina- and Silica-Supported Vanadia Revisited: An Experimental and Theoretical Model Catalyst Study. *J. Catal.* **2004,** *226*, 88-100.

12. Nitsche, D.; Hess, C., Structure of Isolated Vanadia and Titania: A Deep UV Raman, UV-Vis, and IR Spectroscopic Study. *J. Phys. Chem. C* **2016,** *120*, 1025-1037.
13. Tian, H. J.; Wachs, I. E.; Briand, L. E., Comparison of UV and Visible Raman Spectroscopy of Bulk Metal Molybdate and Metal Vanadate Catalysts. *J. Phys. Chem. B* **2005,** *109*, 23491-23499.
14. Wachs, I. E., Catalysis Science of Supported Vanadium Oxide Catalysts. *Dalton Trans.* **2013,** *42*, 11762-11769.
15. Waleska, P.; Rupp, S.; Hess, C., Operando Multiwavelength and Time-Resolved Raman Spectroscopy: Structural Dynamics of a Supported Vanadia Catalyst at Work. *J. Phys. Chem. C* **2018,** *122*, 3386-3400.
16. Waleska, P. S.; Hess, C., Oligomerization of Supported Vanadia: Structural Insight Using Surface-Science Models with Chemical Complexity. *J. Phys. Chem. C* **2016,** *120*, 18510-18519.
17. Weckhuysen, B. M.; Keller, D. E., Chemistry, Spectroscopy and the Role of Supported Vanadium Oxides in Heterogeneous Catalysis. *Catal. Today* **2003,** *78*, 25-46.
18. Wu, Z., Multi-Wavelength Raman Spectroscopy Study of Supported Vanadia Catalysts: Structure Identification and Quantification. *Chin. J. Catal.* **2014,** *35*, 1591-1608.
19. Wu, Z.; Kim, H.-S.; Stair, P. C.; Rugmini, S.; Jackson, S. D., On the Structure of Vanadium Oxide Supported on Aluminas: UV and Visible Raman Spectroscopy, UV-Visible Diffuse Refectance Spectroscopy, and Temperature-Programmed Reduction Studies. *J. Phys. Chem. B* **2005,** *109*, 2793-2800.
20. Langeslay, R. R.; Kaphan, D. M.; Marshall, C. L.; Stair, P. C.; Sattelberger, A. P.; Delferro, M., Catalytic Applications of Vanadium: A Mechanistic Perspective. *Chem. Rev.* **2019,** *119*, 2128-2191.
21. Gao, Z.; Dong, M.; Wang, G.; Sheng, P.; Wu, Z.; Yang, H.; Zhang, B.; Wang, G.; Wang, J.; Qin, Y., Multiply Confined Nickel Nanocatalysts Produced by Atomic Layer Deposition for Hydrogenation Reactions. *Angew. Chem. Int. Ed. Engl.* **2015,** *54*, 9006-9010.
22. Hess, C.; Schlögl, R., Nanostructured Catalysts: Selective Oxidations. *RSC Nanosci. Nanotechnol.* **2011,** *19*.
23. Reddy, B. M.; Mehdi, S.; Reddy, E. P., Dispersion and Thermal-Stability of Vanadium-Oxide Catalysts Supported on Titania Silica Mixed-Oxide. *Catal. Lett.* **1993,** *20*, 317-327.

24. Roozeboom, F.; Mittelmeijerhazeleger, M. C.; Moulijn, J. A.; Medema, J.; Debeer, V. H. J.; Gellings, P. J., Vanadium-Oxide Monolayer Catalysts .3. A Raman-Spectroscopic and Temperature-Programmed Reduction Study of Monolayer and Crystal-Type Vanadia on Various Supports. *J. Phys. Chem.* **1980,** *84*, 2783-2791.
25. Gao, Z.; Qin, Y., Design and Properties of Confined Nanocatalysts by Atomic Layer Deposition. *Acc. Chem. Res.* **2017,** *50*, 2309-2316.
26. O'Neill, B. J.; Jackson, D. H. K.; Lee, J.; Canlas, C.; Stair, P. C.; Marshall, C. L.; Elam, J. W.; Kuech, T. F.; Dumesic, J. A.; Huber, G. W., Catalyst Design with Atomic Layer Deposition. *ACS Catal.* **2015,** *5*, 1804-1825.
27. Zhang, B.; Qin, Y., Interface Tailoring of Heterogeneous Catalysts by Atomic Layer Deposition. *ACS Catal.* **2018,** *8*, 10064-10081.
28. Ruff, P.; Carillo-Solano, M.; Ulrich, N.; Hadley, A.; Kluth, P.; Toimil-Molares, M. E.; Trautmann, C.; Hess, C., Nanoscale Structuring in Confined Geometries using Atomic Layer Deposition: Conformal Coating and Nanocavity Formation. *Z. Phys. Chem.* **2018,** 232, 1147–1171.
29. Ruff, P.; Lauterbach, S.; Kleebe, H.-J.; Hess, C., Surface Structuring of Mesoporous Materials by Controlled Synthesis of Nanocavities. *Microp. Mesop. Mater.* **2016,** *235*, 160-169.
30. Sobel, N.; Hess, C., Nanoscale Structuring of Surfaces by Using Atomic Layer Deposition. *Angew. Chem. Int. Ed. Engl.* **2015,** *54*, 15014-15021.
31. Lu, J.; Elam, J. W.; Stair, P. C., Synthesis and Stabilization of Supported Metal Catalysts by Atomic Layer Deposition. *Acc. Chem. Res.* **2013,** *46*, 1806-1815.
32. Lu, J. L.; Liu, B.; Greeley, J. P.; Feng, Z. X.; Libera, J. A.; Lei, Y.; Bedzyk, M. J.; Stair, P. C.; Elam, J. W., Porous Alumina Protective Coatings on Palladium Nanoparticles by Self-Poisoned Atomic Layer Deposition. *Chem. Mater.* **2012,** *24*, 2047-2055.
33. Dungen, P.; Greiner, M.; Bohm, K. H.; Spanos, I.; Huang, X.; Auer, A. A.; Schlogl, R.; Heumann, S., Atomically Dispersed Vanadium Oxides on Multiwalled Carbon Nanotubes via Atomic Layer Deposition: A Multiparameter Optimization. *J. Vac. Sci. Technol. A* **2018,** *36*, 01A126.
34. Herrera, J. E.; Isimjan, T. T.; Abdullahi, I.; Ray, A.; Rohani, S., A Novel Nanoengineered VO_x Catalyst Supported on Highly Ordered TiO_2 Nanotube Arrays for Partial Oxidation Reactions. *Appl. Catal. A* **2012,** *417*, 13-18.

35. Keranen, J.; Guimon, C.; Liskola, E.; Auroux, A.; Niinisto, L., Atomic Layer Deposition and Surface Characterization of Highly Dispersed Titania/Silica-Supported Vanadia Catalysts. *Catal. Today* **2003,** *78*, 149-157.

36. Wu, W. Q.; Ding, K. L.; Liu, J.; Drake, T.; Stair, P.; Weitz, E., Methanol Oxidation to Formate on ALD-Prepared VO_x/theta-Al_2O_3 Catalysts: A Mechanistic Study. *J. Phys. Chem. C* **2017,** *121*, 26794-26805.

37. Chen, J.; Li, Y. R.; Huang, L.; Li, C.; Shi, G. Q., High-Yield Preparation of Graphene Oxide From Small Graphite Flakes via an Improved Hummers Method With a Simple Purification Process. *Carbon* **2015,** *81*, 826-834.

38. Sobel, N.; Hess, C.; Lukas, M.; Spende, A.; Stuhn, B.; Toimil-Molares, M. E.; Trautmann, C., Conformal SiO_2 Coating of Sub-100 nm Diameter Channels of Polycarbonate Etched Ion-Track Channels by Atomic Layer Deposition. *Beilstein J. Nanotechnol.* **2015,** *6*, 472-479.

39. Gloskovskii, A.; Nepijko, S. A.; Schonhense, G.; Therese, H. A.; Reiber, A.; Kandpal, H. C.; Fecher, G. H.; Felser, C.; Tremel, W.; Klimenkov, M., Spectroscopic and Microscopic Study of Vanadium Oxide Nanotubes. *J. Appl. Phys.* **2007,** *101*, 084301.

40. Gallasch, T.; Stockhoff, T.; Baither, D.; Schmitz, G., Ion Beam Sputter Deposition of V_2O_5 Thin Films. *J. Power Sources* **2011,** *196*, 428-435.

41. Marcano, D. C.; Kosynkin, D. V.; Berlin, J. M.; Sinitskii, A.; Sun, Z. Z.; Slesarev, A.; Alemany, L. B.; Lu, W.; Tour, J. M., Improved Synthesis of Graphene Oxide. *ACS Nano* **2010,** *4*, 4806-4814.

42. Shen, J. F.; Yan, B.; Shi, M.; Ma, H. W.; Li, N.; Ye, M. X., One Step Hydrothermal Synthesis of TiO_2-Reduced Graphene Oxide Sheets. *J. Mater. Chem.* **2011,** *21*, 3415-3421.

43. Shi, Q. Q.; Li, Y.; Zhou, Y.; Miao, S.; Ta, N.; Zhan, E. S.; Liu, J. Y.; Shen, W. J., The Shape Effect of TiO_2 in VO_x/TiO_2 Catalysts for Selective Reduction of NO by NH_3. *J. Mater. Chem. A* **2015,** *3*, 14409-14415.

44. Wachs, I. E., Raman and IR Studies of Surface Metal Oxide Species on Oxide Supports: Supported Metal Oxide Catalysts. *Catal. Today* **1996,** *27*, 437-455.

45. Kim, H.-S.; Stair, P. C., Resonance Raman Spectroscopic Study of Alumina-Supported Vanadium Oxide Catalysts with 220 and 287 nm Excitation. *J. Phys. Chem. A* **2009,** *113*, 4346-4355.

46. Wu, Z.; Stair, P. C.; Rugmini, S.; Jackson, S. D., Raman Spectroscopic Study of V/theta-Al_2O_3 Catalysts: Quantification of Surface Vanadia Species and Their Structure Reduced by Hydrogen. *J. Phys. Chem. C* **2007,** *111*, 16460-16469.
47. Weber, A.; Mcginnis, E. A., The Raman Spectrum of Gaseous Oxygen. *J. Mol. Spectr.* **1960,** *4*, 195-200.
48. Hess, C.; Tzolova-Müller, G.; Herbert, R., The Influence of Water on the Dispersion of Vanadia Supported on Silica SBA-15: A Combined XPS and Raman Study. *J. Phys. Chem. C* **2007,** *111*, 9471-9479.
49. Nitsche, D.; Hess, C., In Situ Diagnostics of Catalytic Materials Using Tunable Confocal Raman Spectroscopy. *J. Raman Spectr.* **2013,** *44*, 1733-1738.
50. Exarhos, G. J.; Schaaf, J. W., Raman-Scattering from Boron-Nitride Coatings at High-Temperatures. *J. Appl. Phys.* **1991,** *69*, 2543-2548.
51. Andrushkevich, T. V.; Kaichev, V. V.; Chesalov, Y. A.; Saraev, A. A.; Buktiyarov, V. I., Selective Oxidation of Ethanol Over Vanadia-Based Catalysts: The Influence of Support Material and Reaction Mechanism. *Catal. Today* **2017,** *279*, 95-106.
52. Nair, H.; Gatt, J. E.; Miller, J. T.; Baertsch, C. D., Mechanistic Insights Into the Formation of Acetaldehyde and Diethyl Ether From Ethanol Over Supported VO_x, MoO_x, and WO_x Catalysts. *J. Catal.* **2011,** *279*, 144-154.
53. Yun, D. M.; Song, Y.; Herrera, J., Supported Vanadium Oxide Clusters in Partial Oxidation Processes: Catalytic Consequences of Size and Electronic Structure. *ChemCatChem* **2017,** *9*, 3655-3669.
54. Prasai, B.; Cai, B.; Underwood, M. K.; Lewis, J. P.; Drabold, D. A., Properties of Amorphous and Crystalline Titanium Dioxide From First Principles. *J. Mat. Sci.* **2012,** *47*, 7515-7521.
55. Samek, I. A.; Bobbitt, N. S.; Snurr, R. Q.; Stair, P. C., Interactions of VO_x Species With Amorphous TiO_2 Domains on ALD-Derived Alumina-Supported Materials. *J. Phys. Chem. C* **2018,** *123*, 7988-7999.
56. Gao, X. T.; Wachs, I. E., Molecular engineering of supported vanadium oxide catalysts through support modification. *Top. Catal.* **2002,** *18*, 243-250.